*Article*

# A Transient Seepage–Thermal Stability Model for Cohesionless Soil Slopes in the Semi-Arid Continental Climate of the Canadian Prairies

Ilyas Akram and Shahid Azam *

Environmental Systems Engineering, Faculty of Engineering Applied Science, University of Regina, 3737 Wascana Parkway, Regina, SK S4S 0A2, Canada
* Correspondence: shahid.azam@uregina.ca

**Abstract:** Seasonal weather variations have a profound effect on the integrity of cohesionless soil slopes in the Canadian Prairies owing to the prevalent semi-arid continental climate. The primary contribution of this research is the development of a transient and two-dimensional stability model that is fully coupled with hydraulic and thermal flows. The model was used to predict the factor of safety (*FS*) for two slope geometries (18 m height and 26 m height) subjected to three weather scenarios (mean, extreme wet, and extreme dry) and four ponding combinations on the upstream and downstream sides of the slopes under no-load and train-load conditions. Results indicated that for mean climate conditions, *FS* trends fluctuate till April, followed by an increase that remains constant up to November and decreases thereafter. Generally, the *FS* shows subdued fluctuations and higher values for the high slope compared with the low slope. For wet climate conditions, the *FS* patterns are similar to mean conditions, albeit with reduced durations of stability during summer. For dry climate conditions, *FS* values are higher than mean conditions and nearly constant for most of the year. For no ponding and downstream ponding, *FS* > 1 throughout the year. In contrast, *FS* > 1 only during the summer (with reduced time in wet climate and extended time in dry climate conditions) for upstream ponding and upstream–downstream ponding. For train loading, *FS* shows subdued fluctuations and lower values than the corresponding no-loading scenarios for both slopes. The effects of climate conditions and ponding scenarios are further reduced for the high slope. These findings are useful for decision making with regard to the initial design and ongoing performance of natural slopes and embankments in the cohesionless soils of the region.

**Keywords:** seasonal weather; cohesionless soils; slope stability; transient modeling

## 1. Introduction

Cohesionless soils are widely distributed around the globe and constitute about 10% of the total land area of the world [1]. These soils are abundantly found in arid and semi-arid regions (above and below the tropical zone), including central and south Asia, the Middle East and northern Africa, North and South America, and Australia [2]. In such regions, annual evaporation is generally more than precipitation and, as such, these cohesionless soils have low water content for most of the year [3]. Excessive dryness results in a meta-stable structure where soil particles are held together mainly through interparticle bonding of suction [4]. During precipitation, water infiltrates into the soil to remove suction bonding, thereby reducing the shear strength of the soil [5]. Alternate saturation and desaturation processes render the soil slopes susceptible to distress and eventual failure. For instance, the safety factor of the Afsluitdijk boundary dam in the Netherlands has significantly decreased over the last 80 years due to surface erosion, cracking, and subsidence [6,7]. Furthermore, the impact of climate change in the form of rising temperature and extreme precipitation [8,9] results in heat waves, droughts, and flash floods, thereby potentially increasing the occurrence of geohazards globally [10]. Such extreme conditions lead to the

failure of even natural slopes to block exiting rivers to form landslide dams [11]. Recent examples include Attabad, Pakistan [12] and Oso, United States of America [13]. Since arid and semi-arid regions form 41% of the continental earth surface, where 30% population of the world resides [14–16], it is of utmost importance to evaluate the slope stability of cohesionless soil in such regions.

The environmental impacts of slope instability incidents include the following: (i) damage to civil infrastructure networks (pipelines, highways/bridges) in natural slopes and abutments; (ii) loading of downstream water bodies with sediments in hydraulic dams; (iii) contamination of rivers in case of above-ground tailings storage facilities; (iv) wiping out of forests to remove protection to soil erosion; (v) changing surface morphology along with loose sediment deposition; and (vi) loss of life and property [17–20]. In addition, the Canadian Prairies have unique topographical features ranging from rolling hills to plateaus and broad undulating plains [21], and the region is significantly affected by climate change. For example, the large scale flooding of 2011 in Manitoba and Saskatchewan and of 2013 in Alberta occurred due to spring snow melt and summer rainfall [22,23]. Likewise, about two-thirds of the area is exposed to droughts due to prolonged dry periods [24]. This means that most earth structures (such as 90 hydraulic dams [25], 65 tailings dams [26], and about 500 saline lakes [27]) are vulnerable to failure, with potentially disastrous consequences. Clearly, there is a need to develop sustainable (cost-effective, environmentally friendly, and safe for the public) civil infrastructure in the region to meet the requirements of the Public Infrastructure Engineering Vulnerability Committee (PIEVC) protocol.

Seasonal moisture variations especially affect cohesionless soils owing to the porous nature of such soils [28]. Slope instability in transportation networks and pipeline systems costs an average of CAD 125 million in direct damages to infrastructure and another CAD 210 million in preventive measures each year [29]. The number and frequency of catastrophic events due to washout of the supporting earthen materials are increasing, as evidenced by the following examples: derailment of trains containing dangerous goods at Gainford, Alberta [30]; removal of a 150-m section of slope toe at Frenchman Valley, Saskatchewan [31]; and bursting of a natural gas pipeline near Otterburne, Manitoba [32]. Dams are particularly vulnerable because the stored water raises the phreatic surface in the earth structures. The Bossano Dam in Alberta was severely damaged by the 2013 high floods and underwent major repair work costing CAD 100 million [33]. Likewise, the Rivers dam in Manitoba was unable to accommodate the heavy inflow following unprecedented rains, thereby forcing 62 downstream communities to evacuate [34]. More than half of the 72 dams in Saskatchewan (La Ronge, Gardiner, Rafferty, and Alameda) require upgrading to protect them from potential failure [35,36]. Furthermore, Saskatchewan has several natural slopes with lakes at the toe end, such as Buena Vista (40 m high) and South Lake (228 m high), which exhibit progressive slope movement, thereby affecting utilities and houses [37,38]. In addition, large-scale construction projects are underway, including the 87-km long canal joining Lake Diefenbaker and Buffalo Pound Lake [39] and the 55-km long Saskatoon Freeway [40]. To ensure the uninterrupted use of existing infrastructure and to support the design of new facilities, there is a need to understand the behavior of cohesionless soils under extreme climatic conditions.

The stability of cohesionless soils under known applied stresses is governed by soil suction (difference of air pressure and water pressure) in the pore network [41]. This parameter depends on soil–atmosphere interactions—that is, decrease due to precipitation or increase due to evaporation [42]. Precipitation results in the downward movement of water to saturate the soil profile by replacing pore air [43]; whereas evaporation causes upward water migration to desaturate the soil profile [44]. These flow processes are also affected by the seasonally variable thermal gradients between the soil and the air. Generally, heat transfer takes place through granular contacts and the water continuum in a saturated state; whereas this process essentially occurs via conduction through soil particles in the desiccated state [45]. During summer, thermal energy moves from the surface downward due to high solar radiation over longer daytime periods [46]. The rise in temperature

increases the pore water pressure in soils primarily due to differences in the coefficients of thermal expansion of pore water and soil solids [47]. During winter, heat is removed from the soil because of the low air temperature in comparison to that of the soil [48]. This results in water freezing in surface pores and the attraction of water from the lower unfrozen pores, along with desaturation from the bottom upwards [49]. It is clear that the hydraulic and heat flow processes must be coupled in order to understand soil behavior under extreme climatic variability. To this end, there is a need to use thermal properties (volumetric heat capacity and thermal conductivity) as functions of volumetric water content that, in turn, is derived from soil–atmosphere interactions.

Conceptually, the coupled flow model generates the water content profile that, in turn, is used as input to determine the safety factor (*FS*) based on a limit equilibrium method. Such models were initially developed for low plastic clays and silty-to-sandy soils using boundary temperature (usually 0 °C, at which water changes phase between liquid and solid) [50–52]. The modeling was improved to take into account the volumetric properties of water and ice [53,54]. These models have been modified to perform transient seepage-thermal-stability analysis by incorporating unsaturated hydraulic properties [55–57], soil thermal properties [58,59], and variable temperatures in the soil profile [60,61]. The improved models have been used for slope stability analysis by considering variable precipitation [62,63], mean annual temperature [59,64], mean climatic conditions for part of the year [61,65], intensity of periodic rainfall [66–68], and variation in air and soil temperature [69,70]. To the authors' knowledge, a comprehensive slope stability modeling comprising transient analysis under extreme climatic conditions has not been conducted.

The main objective of this research was to develop a seepage–thermal stability model for cohesionless soils in a semi-arid continental climate. The model comprised seepage–thermal analysis to obtain the water content profile and slope stability analysis to determine the corresponding *FS*. A parametric study was conducted to evaluate the transient stability of cohesionless soil slopes over one year under mean, extreme wet, and extreme dry climatic conditions.

## 2. Governing Equations

The hydraulic conductivity of soils in a saturated state is constant, while in an unsaturated state, it varies with soil suction [56]. Based on Darcy's law the two-dimensional transient hydraulic flow-through a soil under saturated–unsaturated conditions is expressed as follows [71,72]:

$$\frac{\partial \theta}{\partial t} = \frac{\partial}{\partial x}\left(k_x \frac{\partial H}{\partial x}\right) + \frac{\partial}{\partial y}\left(k_y \frac{\partial H}{\partial y}\right) + Q_w. \tag{1}$$

In the above equation, $\theta$ is volumetric water content; $t$ is time (s); $(k_x)$ and $(k_y)$ are hydraulic conductivities (m/s) in $x$ and $y$ directions, respectively, and considered to be equal (and subsequently identified by $k$); $H$ is total head (m) due to both elevation and soil suction $(\psi)$; and $Q_w$ is the water flux rate through the surface boundary (1/s).

The water in the soil pores freezes as the temperature falls below 0 °C and thaws as soon as the temperature reaches the positive regime. This variation of volumetric water content with temperature through a soil is given as follows [58]:

$$\frac{\partial \theta_u}{\partial T} = \left[\left(\frac{\partial}{\partial x}\left(\lambda_x \frac{\partial T}{\partial x}\right) + \frac{\partial}{\partial y}\left(\lambda_y \frac{\partial T}{\partial y}\right) + Q_T\right) \div \left(L\frac{\partial T}{\partial t}\right)\right] - C_v/L. \tag{2}$$

In the above equation, $\theta_u$ is unfrozen volumetric water content; $T$ is temperature (°C); $(\lambda_x)$ and $(\lambda_y)$ are thermal conductivities (kJ/s/m/°C) in $x$ and $y$ directions, respectively, and assumed to be identical (and later on symbolized by $\lambda$); $Q_T$ is heat flux rate through the surface boundary (kJ/m$^3$·s); $L$ is the latent heat of water for freezing/melting ($334 \times 10^3$ kJ/m$^3$); and $C_v$ is the specific volumetric heat capacity (kJ/m$^3$·°C). The term $\theta_u$ is equal to $\theta$ when the $T \geq 0$ °C and gradually decreases $T < 0$ °C [73].

Equations (1) and (2) were simultaneously solved to determine the transient seepage–thermal flow. The $\theta$ value at a given time (Equation (1)) was used to determine the corresponding values in $\lambda$ and $C_v$ (given later in this paper), which were then used to scale the $\theta$ value with respect to temperature (Equation (2)). Subsequently, the $\theta$ value was used to obtain $\psi$ from the water retention curve (WRC). This is justified because of the marginal difference between suction values from transient analysis and static WRC for cohesionless soils [74,75]. Based on the WRC volumetric water content values ($\theta_r$ for residual and $\theta_s$ for saturated), the extended Mohr–Coulomb failure criteria was used to determine the shear strength ($\tau$) of the soil [76]:

$$\tau = c + \sigma_n tan\varphi' + \psi\left(\frac{\theta - \theta_r}{\theta_s - \theta_r}\right) tan\varphi' .$$ (3)

In the above equation, $c$ is cohesion (kPa); $\varphi'$ is friction angle; and $\sigma_n$ is normal stress (self-weight of soil) (kPa) [77]. The normal stress is in the vertical direction, and the shear force per unit area is calculated in the horizontal direction [78].

Theoretically, freezing–thawing is identical to drying–wetting [79]. An atmospheric temperature drop results in the downward movement of the freezing front. This means that pore water is frozen above the front and unfrozen below. The thermal gradient develops cryo-suction that attracts the unfrozen water toward the freezing front [80]. This phenomenon increases matric suction in the frozen zone and desaturates the soil from the bottom upward, similar to the drying process [81]. Therefore, the suction values are analogs in both processes for cohesionless soils [82].

Slope stability analysis was conducted using the method of slices. This method divides the entire slope into several slices and calculates the force per unit length at the bottom of each slice by multiplying shear stresses with base length. The Morgenstern–Price (M-P) method satisfies both moment and force equilibria and can be presented in a general form as follows [83]:

$$X = E\,f(x)\,\lambda .$$ (4)

In the above equation, $X$ is the interslice shear force; $E$ is the interslice normal force; $f(x)$ is a function; and $\lambda$ is the scaling factor for $f(x)$ (ratio of applied and specified $f(x)$). To satisfy both force and moment equilibria, the SlopeW module of GeoStudio (2020 version) performed multiple iterations using a defined $f(x)$ (half sine in this study) and a range of $\lambda$ values from $-1.25$ to $1.25$ [78]. The crossover point at a common $\lambda$ was used as the safety factor for a slip surface at a particular time step. Several slip surfaces were automatically generated by defining a range of points using the entry–exit function, and the minimum *FS* value corresponding to the critical slip surface was reported.

## 3. Model Development

### 3.1. Study Area

Figure 1 shows the map of the study area along with the location of the weather station. The total area of Saskatchewan is 651,036 km$^2$ (90.8% land, 9.2% water), with rolling and hilly terrain in the north and vast plains in the south [84]. The study area is important because more than half of the province's population lives here (mostly in Saskatoon, Regina, and Prince Albert) [85], it contains 66 hydraulic dams [36] and 11 potash tailing dams [26], and it is the regional hub for transporting goods to other parts of Canada [86]. The Climate Reference Station of the Saskatchewan Research Council (SRC) in Prince Albert provides reliable data of climatic parameters (air temperature, precipitation, relative humidity, wind speed, solar radiation), which are representative of the typical climate in South Saskatchewan [87]. Furthermore, the weather station records soil temperatures up to 3.0 m depth in silty and sandy soils [88].
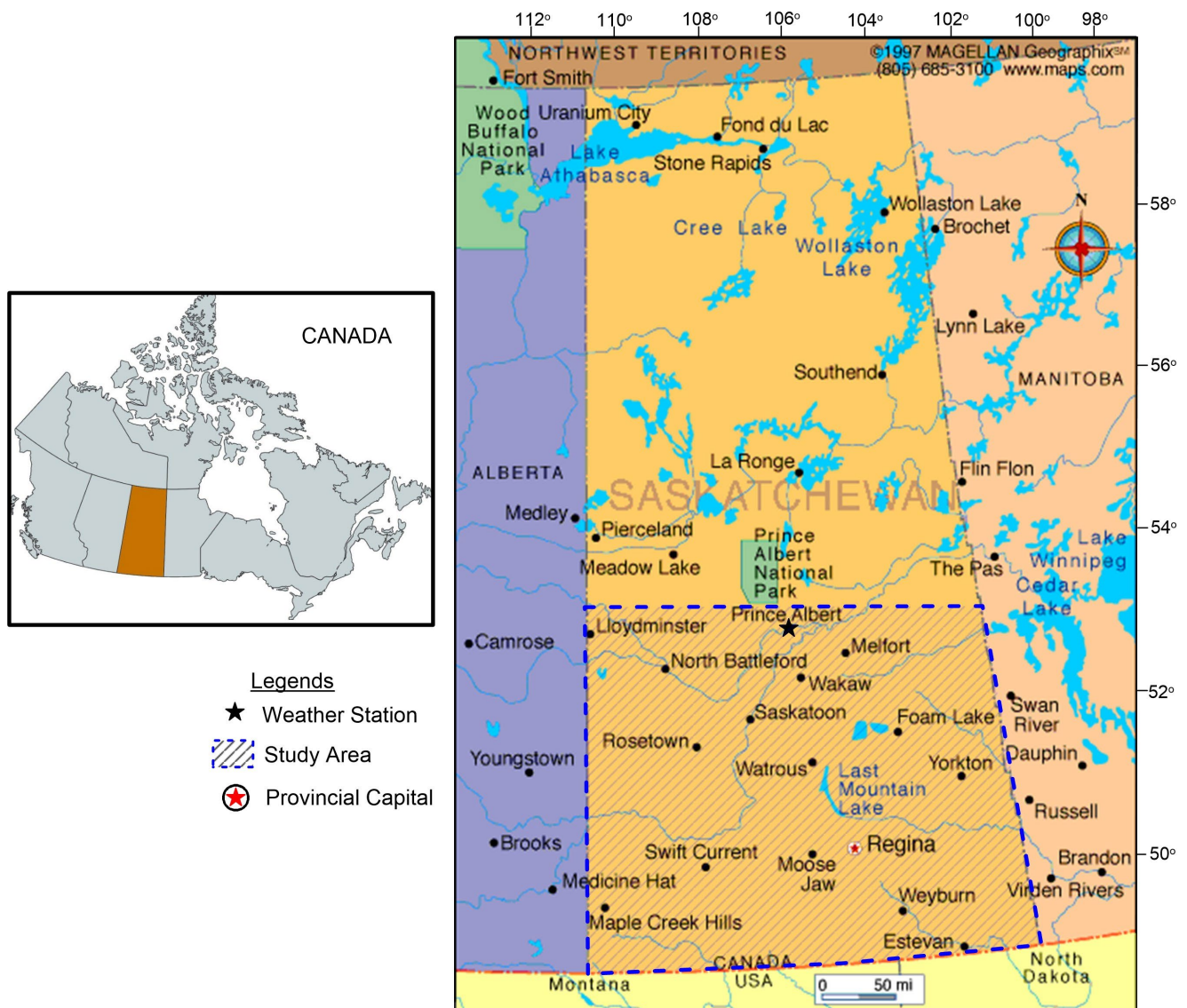
**Figure 1.** Study area and location of the weather station [89,90].

### 3.2. Modeling Scheme

Figure 2 shows the scheme for the transient seepage–thermal stability model. A two-dimensional model was developed to simplify and optimize computational time and mathematical accuracy [91]. Modeling was conducted using the Seep/W and Slope/W modules of the GeoStudio software (2020 version). Typical embankment geometries comprising a slope of 1 V:1.5 H [92] and heights of 18 m and 26 m were modeled (Figure 3).]

The investigated modeling scenarios included regional climate under mean, wet, and dry conditions with each under no ponding (NP), upstream ponding (US), downstream ponding (DS), and ponding at both upstream and downstream (US-DS). To investigate the effect of vehicular loading on embankment stability, the model was run with and without a 70 kN/m applied load on the embankment crest [93]. Each analysis was assigned a code for convenient identification. As example code, M-NP-NL-H stands for mean climate, no ponding, no loading at the crest, and high embankment. All the modeling scenarios are summarized in Table 1.
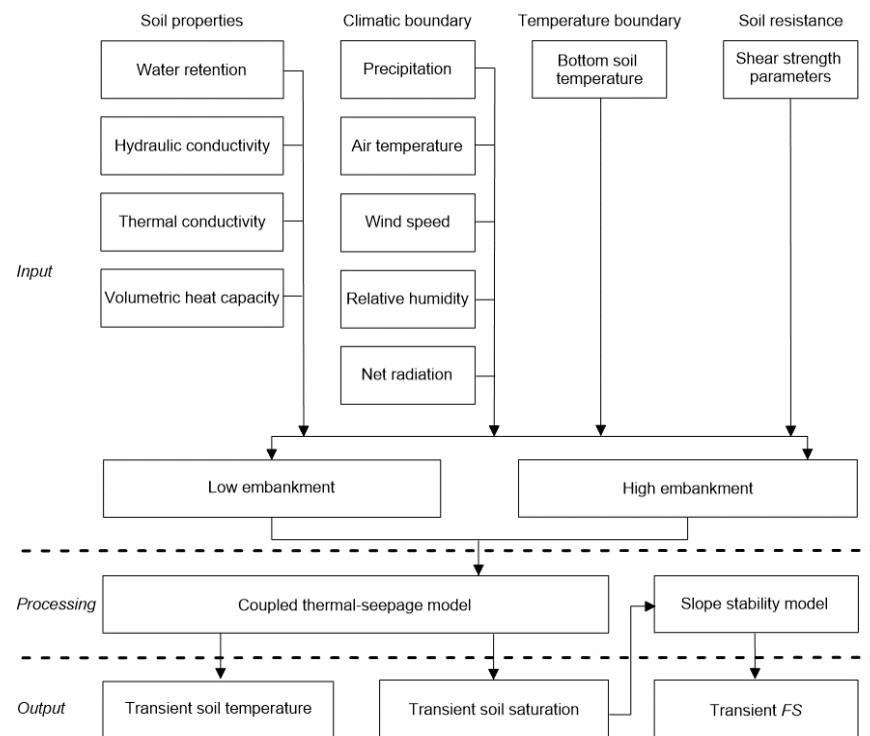
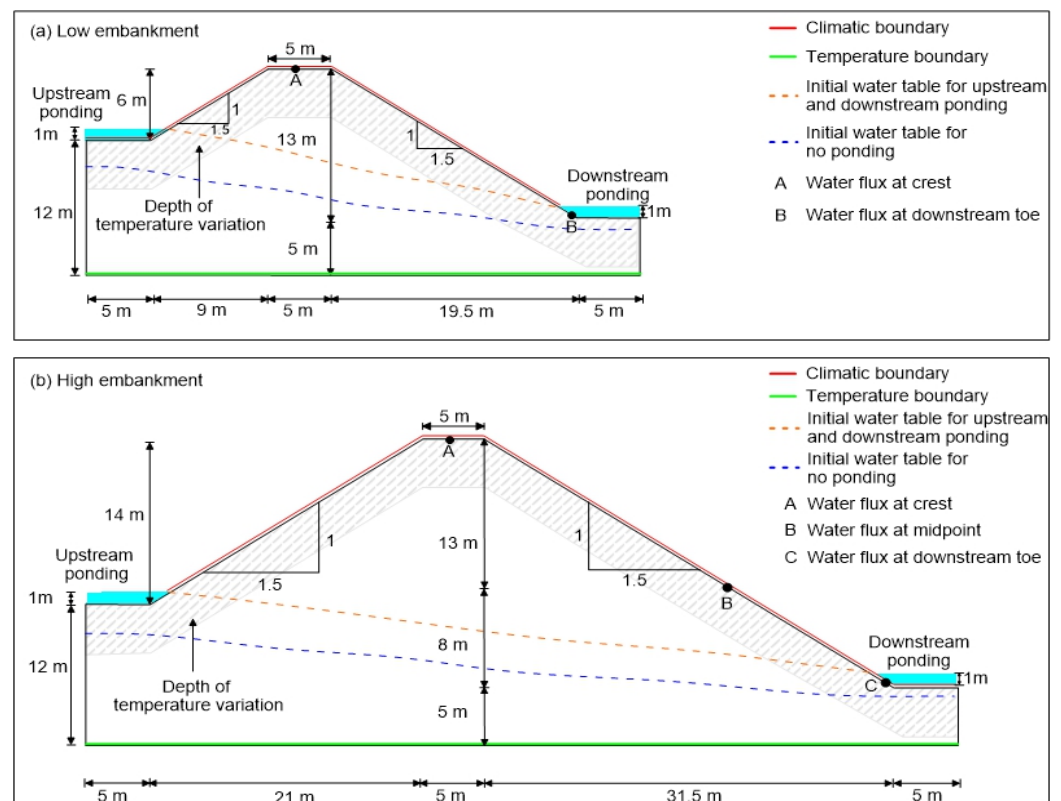**Figure 2.** Modeling scheme for transient seepage–thermal stability analysis.



**Figure 3.** Model geometry for transient seepage–thermal stability analysis under two extreme ponding conditions for (**a**) low embankment and (**b**) high embankment.

**Table 1.** Summary of parametric modeling scenarios and results.

| Climate | Upstream | Downstream | Loading | Geometry | Code |
|---------|----------|------------|---------|----------|------|
| Mean | - | - | - | High | M-NP-NL-H |
|  |  |  |  | Low | M-NP-NL-L |
|  |  |  | 70 kN/m | High | M-NP-TL-H |
|  |  |  |  | Low | M-NP-TL-L |
|  | Ponding | - | - | High | M-US-NL-H |
|  |  |  |  | Low | M-US-NL-L |
|  |  |  | 70 kN/m | High | M-US-TL-H |
|  |  |  |  | Low | M-US-TL-L |
|  | - | Ponding | - | High | M-DS-NL-H |
|  |  |  |  | Low | M-DS-NL-L |
|  |  |  | 70 kN/m | High | M-DS-TL-H |
|  |  |  |  | Low | M-DS-TL-L |
|  | Ponding | Ponding | - | High | M-US-DS-NL-H |
|  |  |  |  | Low | M-US-DS-NL-L |
|  |  |  | 70 kN/m | High | M-US-DS-TL-H |
|  |  |  |  | Low | M-US-DS-TL-L |
| Wet | - | - | - | High | W-NP-NL-H |
|  |  |  |  | Low | W-NP-NL-L |
|  |  |  | 70 kN/m | High | W-NP-TL-H |
|  |  |  |  | Low | W-NP-TL-L |
|  | Ponding | - | - | High | W-US-NL-H |
|  |  |  |  | Low | W-US-NL-L |
|  |  |  | 70 kN/m | High | W-US-TL-H |
|  |  |  |  | Low | W-US-TL-L |
|  | - | Ponding | - | High | W-DS-NL-H |
|  |  |  |  | Low | W-DS-NL-L |
|  |  |  | 70 kN/m | High | W-DS-TL-H |
|  |  |  |  | Low | W-DS-TL-L |
|  | Ponding | Ponding | - | High | W-US-DS-NL-H |
|  |  |  |  | Low | W-US-DS-NL-L |
|  |  |  | 70 kN/m | High | W-US-DS-TL-H |
|  |  |  |  | Low | W-US-DS-TL-L |
| Dry | - | - | - | High | D-NP-NL-H |
|  |  |  |  | Low | D-NP-NL-L |
|  |  |  | 70 kN/m | High | D-NP-TL-H |
|  |  |  |  | Low | D-NP-TL-L |
|  | Ponding | - | - | High | D-US-NL-H |
|  |  |  |  | Low | D-US-NL-L |
|  |  |  | 70 kN/m | High | D-US-TL-H |
|  |  |  |  | Low | D-US-TL-L |
|  | - | Ponding | - | High | D-DS-NL-H |
|  |  |  |  | Low | D-DS-NL-L |
|  |  |  | 70 kN/m | High | D-DS-TL-H |
|  |  |  |  | Low | D-DS-TL-L |
|  | Ponding | Ponding | - | High | D-US-DS-NL-H |
|  |  |  |  | Low | D-US-DS-NL-L |
|  |  |  | 70 kN/m | High | D-US-DS-TL-H |
|  |  |  |  | Low | D-US-DS-TL-L |

The hydraulic and thermal properties of the soil (Figure 5) were assigned to the embankment cross-section. Likewise, the atmospheric parameters (Figure 5) were applied as a climatic boundary and a soil temperature of 5 °C was assigned to the temperature boundary, as explained later in the paper. The cumulative net flux was calculated at the points shown in Figure 3 for both slope geometries. The output of the coupled seepage-thermal model and the shear strength obtained from Equation (3) were used to determine the *FS* and were plotted with respect to time over a one-year timeframe.
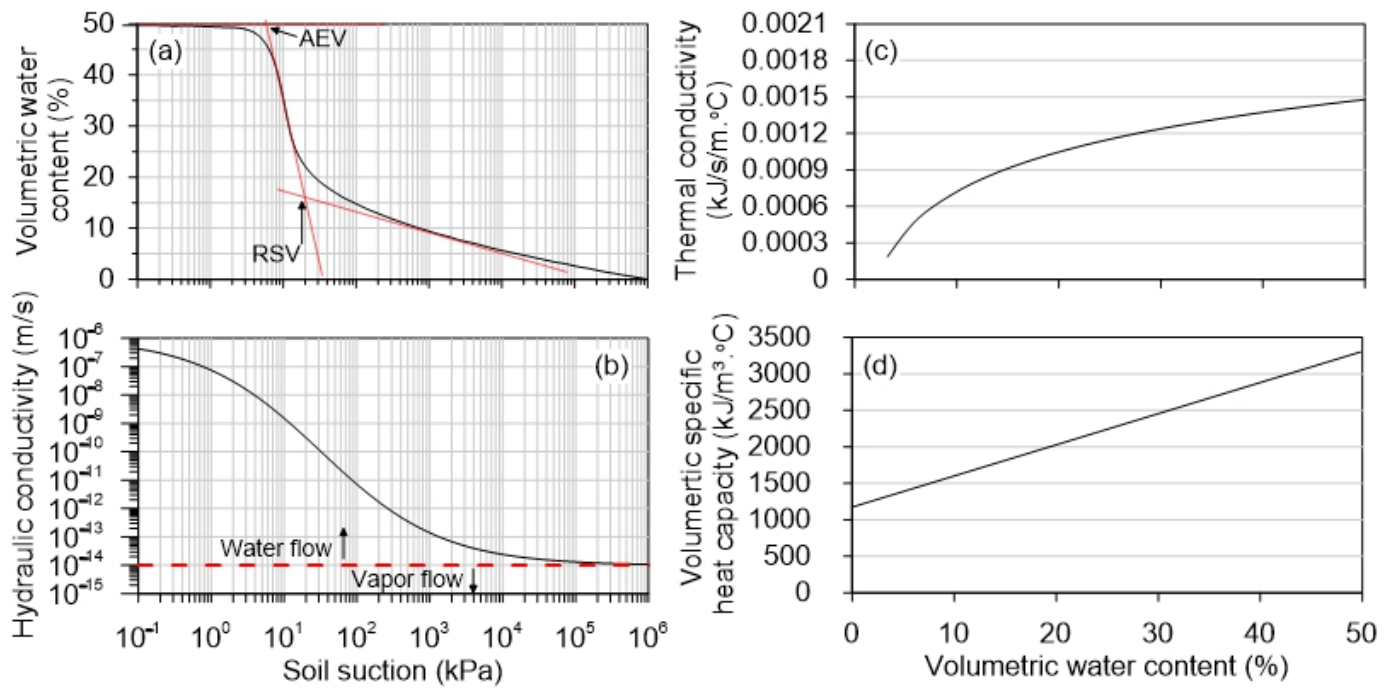


**Figure 4.** Soil property curves: (**a**) water retention; (**b**) hydraulic conductivity; (**c**) thermal conductivity; (**d**) volumetric specific heat capacity.
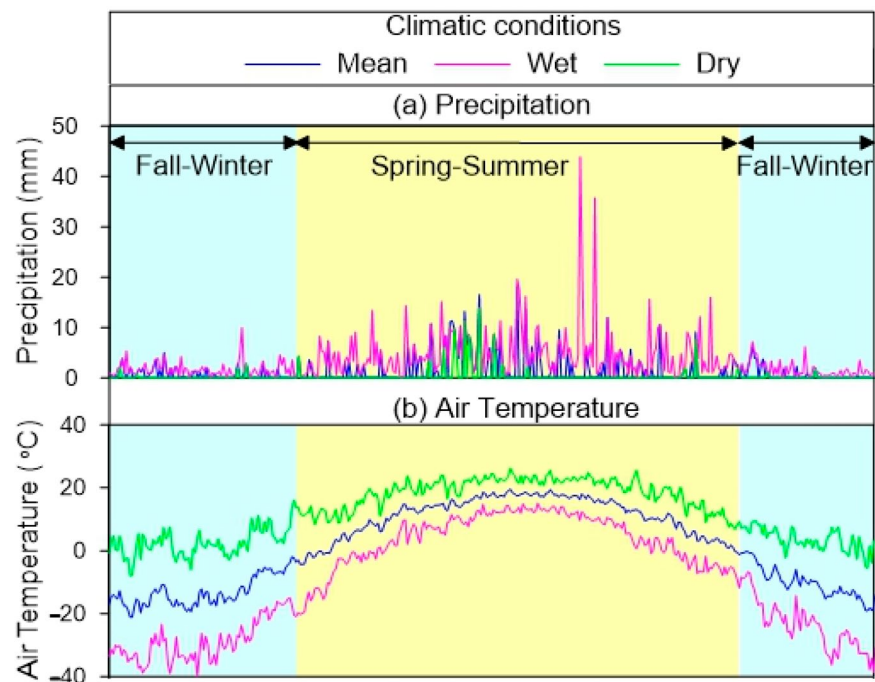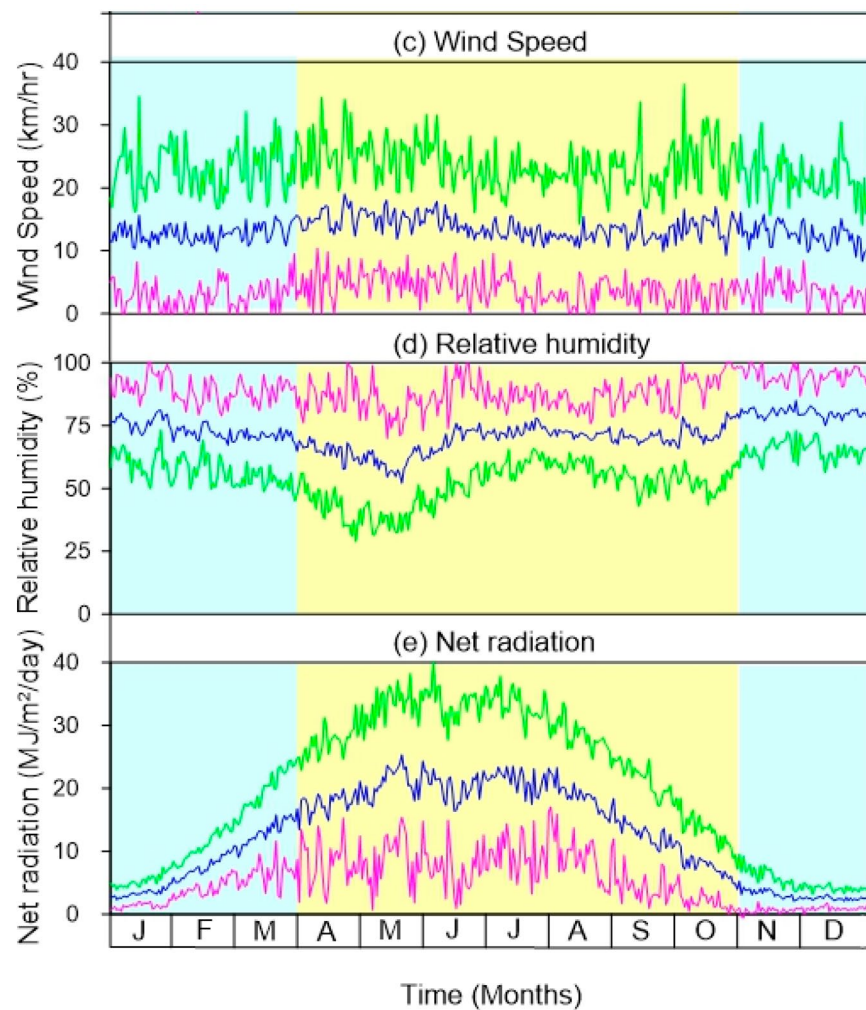


**Figure 5.** *Cont.*

**Figure 5.** Variation of climatic parameters in Southern Saskatchewan, Canada: (**a**) precipitation; (**b**) air temperature; (**c**) wind speed; (**d**) relative humidity; (**e**) net radiation.

*3.3. Soil Properties*

The investigated soil comprised 64% fine sand (material between 4.25 mm and 0.075 mm) and 36% silt (material between 0.075 mm and 0.002 mm), with no clay size fraction (material finer than 0.002 mm) [94]. The moderate consistency (liquid limit ($w_l$) of 27% and plastic limit ($w_p$) of 23%) is associated with the slight affinity of silt particles to water [95]. Overall, the soil was classified as silty sand (SM) according to the Unified Soil Classification System [96]. At the *in-situ* desiccated state, the soil has a $\theta$ of 2.5% and dry unit weight ($\gamma_d$) of 14 kN/m$^3$. Figure 5 shows the hydraulic and thermal parameters of the soil used as input for the flow model. These isotropic soil properties simplify the calculation for the two-dimensional slope model [78]. Based on laboratory test results, Figure 5a shows the WRC that best fitted the following equation [94]:

$$\theta = 0.5 \left[ 1 - \frac{\ln\left(1 + \frac{\psi}{21}\right)}{10.78} \right] \left[ \frac{1}{\ln\left[2.72 + \left(\frac{\psi}{9}\right)^{20}\right]^{0.27}} \right]. \tag{5}$$

Figure 5b shows the hydraulic conductivity ($k$) of the soil for the whole range of suction determined via the wetting front method and fitted with the following equation [94]:

$$k = 10^{\frac{1 + 5\exp\ (-1.2\log\psi\ + 0.2)}{8}} \div 10^6. \tag{6}$$

Figure 5c shows the thermal conductivity ($\lambda$) of soil (kJ/s/m/°C) plotted with respect to $\theta$ as calculated through the following equation modified after [50,52,97] using constant parameters for the investigated soil:

$$\lambda = 1.47 \times 10^{-4} - 0.025\left[\left(0.85\log\left(\frac{\theta}{0.46}\right) + 1\right) - 1\right]. \tag{7}$$

Figure 5d shows the specific volumetric heat capacity ($C_v$) of the soil with respect to the volumetric water content given by the following equation [98]:

$$C_v = 0.0006 + 4.184\theta. \tag{8}$$

The reported shear strength parameters ($c = 0$ and $\varphi' = 42°$) for intact cohesionless soil under full saturation was used [99]. The unsaturated shear strength parameters were estimated using Equation (3).

*3.4. Climate Parameters*

The surface soils in Canadian Prairies experience a net water deficit for most of the year because evaporation generally exceeds precipitation. The total annual potential evaporation across the region is ~600 mm (400 mm in Manitoba to 1000 mm in Alberta [100]) compared to the total annual precipitation of ~500 mm (275 mm in Manitoba to 1000 mm in Alberta [101]). Furthermore, extreme seasonal variability in meteorological parameters persists in the area [102]. The average temperature ranges from −4 °C to −13 °C in winter (November–March) and 4 °C to 16 °C in summer (April–October). About 40% of the precipitation is received as winter snow and the remainder as summer rainfall [103]. The snow dump of $1.3 \pm 0.1$ m [104] melts in spring such that about 80% of the resulting water is drained as surface runoff depending on soil permeability and antecedent desaturation [105,106]. In summer, high solar radiation of ~25 MJ/m²/day [107] and long daytime exposure, along with a wind speed of ~16 km/h [108], ensure that about 90% of the rainfall received at the ground evaporates back to the atmosphere, thereby leading to desiccated surface soils except during rainfall events and shortly thereafter [109,110]. In winter, sub-zero air temperature decreases the soil temperature to freeze the pore water, although this process is subdued because of the preceding water deficit in the soil. The 10-year climate data from southern Saskatchewan indicates a frozen depth of up to 0.5 m during December–February [103].

The climate of southern Saskatchewan is broadly classified as *Dfb* (humid continental) as per the Köppen–Geiger classification system [111]. This region experiences extreme seasonal variations, from warm summers to cold winters, with overall semi-arid weather [102]. In the climate symbol, the letter *D* stands for the average air temperature above 10 °C over five months and below 3 °C in the coldest month; *f* stands for precipitation larger than 0 mm in all months; and b represents all monthly average air temperatures below 22 °C [112]. Such seasonal variations, along with increasing flash floods and long droughts due to global warming in the region [112,113], result in alternate saturation–desaturation, causing serious concern for slope stability.

Figure 5 shows the 10-year (2011–2020) average annual climate parameters at the Prince Albert weather station [103], which represent the typical climate of southern Saskatchewan. Statistical analyses were conducted to obtain mean values from the daily data. From the mean data, the daily standard deviation values were calculated to determine 95% confidence intervals for each of the climate parameters to obtain extreme values. These values were used to obtain dry conditions comprising minimum precipitation, maximum temperature, maximum wind, minimum humidity, and maximum radiation and wet conditions, with the opposite values for atmospheric parameters. Additional possible combinations resulting in dry and wet conditions were not considered. A similar approach was used by [114] to model the seepage–thermal behavior of a glacial till under extreme climatic conditions by averaging the 10-year climate data.

The standardized precipitation and evapotranspiration index (SPEI) was used to define the wet, dry, and mean climatic conditions. The SPEI was calculated by using cumulative precipitation and evaporation data following the method of [115]. The SPEI values were used to classify the climatic conditions as follows: mean (0.03 to 0.23), wet (1.01 to 1.2), and dry (−1.2 to −1.3). The calculated SPEI values correlated well with the criteria proposed by [116] for mean (between −1 and 1), wet (≥1), and dry (≤−1).

Based on mean values, the climate was divided into fall–winter (November to March), when the temperature was below 0 °C, and spring–summer (April to October) when the temperature was above 0 °C. The daily precipitation (Figure 5a) demonstrates that spring–summer rainfall occurs for 106 days in mean conditions, 21 days in dry conditions, and 279 days in wet conditions. The fall–winter precipitation was received and accumulated as snow, which melts during spring–summer as the temperature rises above 0 °C. Likewise, Figure 5b shows that daily air temperature remains above 0 °C for 192 (mean), 329 (dry conditions), and 138 days (wet conditions). The number of days with temperatures above 0 °C corroborated well with the semi-arid climate of the region [112]. Further, the mean and dry climatic conditions were classified as *Dfb* (similar to the regional climate); whereas the wet climate was classified as *Dfc* (continental subarctic climate) [117].

The wind speed (Figure 5c) exhibits fluctuation throughout the year, and average annual values are calculated for the mean (13 km/h), dry (23 km/h), and wet (4 km/h) conditions. Figure 5d shows the spring–summer average relative humidity of 69% (mean), 51% (dry conditions), and 87% (wet conditions). The corresponding values of relative humidity during winters increase to 77 (mean), 61 (dry), and 92% (wet). Similarly, Figure 5e shows that spring–summer has an average net radiation of 17 MJ/m$^2$/day (mean), 27 MJ/m$^2$/day (dry), and 7 MJ/m$^2$/day (wet); whereas the corresponding fall–winter values for the similar conditions are 5, 8, and 2 MJ/m$^2$/day, respectively. The climatic parameters corresponding to each condition were directly incorporated into the model, whereas snow accumulation or melting was estimated using precipitation and air temperature data.

*3.5. Ground Temperature*

Based on 10-year (2011~2020) data, the average soil temperature profile measured at the above site exhibited a fluctuation between −5 °C and 18 °C, which reduced with increasing depth [103]. Based on linear extrapolation [114], a 4.2 m depth (at a temperature of 5 °C) was used as the bottom thermal boundary. Beyond this depth, the soil was assumed to be unaffected by weather variations [58,60]. A spatial thermal function was defined to train the model to consider the variation in temperature up to 4.2 m, beyond which it was unchanged up to the bottom boundary.

## 4. Results and Discussion

Figure 6 shows a comparison of predicted and measured monthly soil temperatures at different depths to validate the accuracy of the model. The measured and predicted ground temperatures corroborated well with each other, with a mean absolute error (MAE) between 0.7 and 1.2 and a root mean square error (RSME) between 0.9 and 1.4 for all depths. The data fell within a half standard deviation on both sides of the equality line, with a coefficient of determination ($R^2$) equal to 0.88. An $R^2$ value higher than 0.81 is considered a strong correlation between measured and predicted values [118–120]. The field data were obtained from Prince Albert weather station, with a silty soil closely matching the investigated material [103]. Such soils have a hydraulic conductivity range of $10^{-5}$ to $10^{-7}$ m/s [86,94] and a thermal conductivity range of 0.0007 to 0.0029 kJ/s/m·°C [121,122]. The hydraulic (Figure 5b) and thermal (Figure 5c) properties of the investigated soil fell within the above range and, as such, the model was considered to adequately capture field conditions. Therefore, the transient seepage–thermal model is applicable in determining the stability of the slopes in the region.
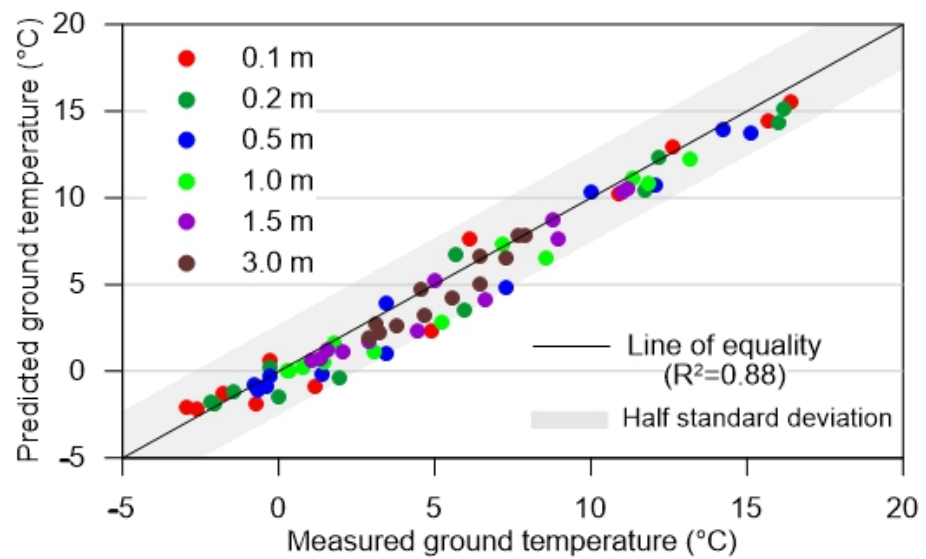
**Figure 6.** Comparison of predicted and measured monthly soil temperatures.

Figure 7 compares the transient measured and predicted changes in ground temperature up to 3.0 m depth. The predicted data correlated well with the measured in situ soil temperature at all the depths. At depths of 0.1 to 0.5 m, the soil temperature remained below 0 °C from January to April, gradually increased to reach a maximum in July, and subsequently decreased to fall below 0 °C by October, remaining constant thereafter. This implies that the embankment surface experiences fluctuations in water content due to freeze–thaw. In contrast, the soil temperature remained close to 0 °C at 1 m depth from January to April, gradually increasing until August, followed by a drop, yet nonetheless remaining above 0 °C. Likewise, at a depth of 1.5 m and beyond, the temperature remained in the positive range throughout the year. This is because the effect of seasonal variation reduces with depth due to the thermal conduction and isolation of deeper soil layers from the atmosphere [123–125].
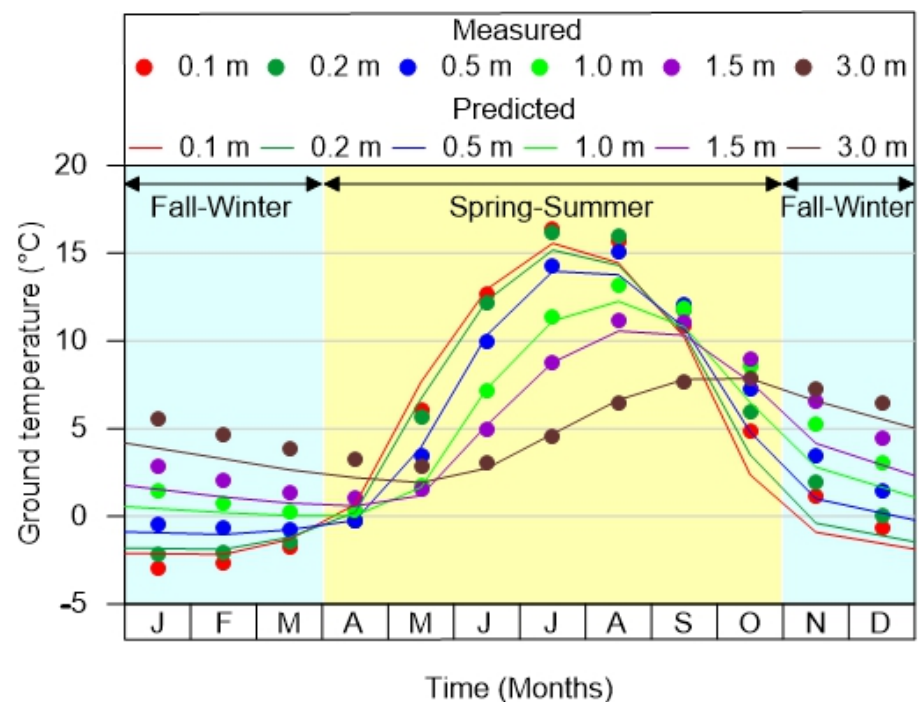


**Figure 7.** Variation of predicted and measured soil temperatures with time.

Figure 8 shows the transient *FS* at the downstream slope under different climatic conditions applied to the low embankment (Figure 3a) for various ponding and loading scenarios (Table 1). Results of the downstream slope are given because this face is more vulnerable to failure compared to the upstream slope as water movement from higher to lower elevations and larger slope length result in increased unsupported span [126]. The line for *FS* = 1 differentiates between a safe (above) and failed (below) slope. The various pairs of scenarios under mean climate conditions indicated the following observations. For NP-NL (Figure 8a), *FS* fluctuated between 1.35 and 1.25 till April, followed by an increase to 1.5 till October, and was reduced to 1.35 thereafter. The higher values during spring–summer are attributed to increased suction because evaporation is more than precipitation. Under the same conditions with TL (Figure 8b), *FS* was reduced to 1.0 and remained unchanged for the entire year because of increased sliding moment due to train loading [127]. For US-NL (Figure 8c), *FS* was around 0.3 till mid-May, followed by an abrupt jump to reach 1.25, remaining constant till early November, and falling to 0.75 around that time, being gradually reduced to 0.3 by the end of December. The lower *FS* values are attributed to increased saturation of the slope due to the higher water table generated by upstream ponding [128]. A comparison of upstream to downstream ponding indicated that slopes are 58% more susceptible to failure in the upstream ponding condition owing to a high phreatic surface [129]. Furthermore, upstream ponding was reported to be the prime reason for slope instability at Hudson Bay and Ponton, Canada [130]. Under the same conditions with TL (Figure 8d), the *FS* pattern was identical such that the slope always failed. For DS-NL (Figure 8e), *FS* fluctuated between 1.35 and 1.5, following a trend similar to NP-NL (Figure 8a) because downstream ponding drains without affecting the saturation of the entire slope. Under the same conditions with TL (Figure 8f), *FS* remained close to 1.0 (similar to Figure 8b). For US-DS-NL (Figure 8g), the *FS* trend was similar to US-NL because saturation was predominant due to ponding on both sides of the slope. Under the same conditions with TL (Figure 8h), the *FS* trend was the same as before and the slope always failed due to increased loading.

The wet climate was imposed by using maximum precipitation, minimum temperature, minimum wind speed, maximum humidity, and minimum radiation. The various pairs of scenarios under wet climate conditions resulted in the following. For NP-NL (Figure 8a), the initial *FS* fluctuation extended by two months till end of June (due to saturated conditions arising from excess precipitation compared to evaporation), followed by an increase up to 1.5 (similar to mean climate conditions) till the end of September, an abrupt change to 1.1 during October (because lower the temperature reduces evaporation, thereby ensuring close to saturation), and a gradual reduction to 0.9 by the end of December (owing to continuous temperature reduction). Under the same conditions with TL (Figure 8b), the *FS* trend and values were quite similar to mean climate conditions (increased sliding moment), along with a reduction in resistance due to the collapse of the soil structure in wet climate conditions [99]. For US-NL (Figure 8c), the trends and *FS* values are similar to their counterparts for mean climate conditions such that the period for *FS* < 1 was extended till the end of June, and the period for *FS* > 1 was reduced till the end of September; the reasons for these observations are the same as before. Under the same conditions with TL (Figure 8d), the *FS* trend was similar to mean climate conditions, with a reduced duration of *FS* close to 1, again due to the above-mentioned reasons. For DS-NL (Figure 8e), lower values of *FS* were observed, albeit following a nearly similar trend as that under mean climate conditions. Under the same conditions with TL (Figure 8f), *FS* trends and values were similar to mean climate conditions because of the reasons set out in Figure 9b. Finally, the US-DS for both NL (Figure 8g) and TL (Figure 8h) exhibited nearly similar trends and values to Figure 8c,d.
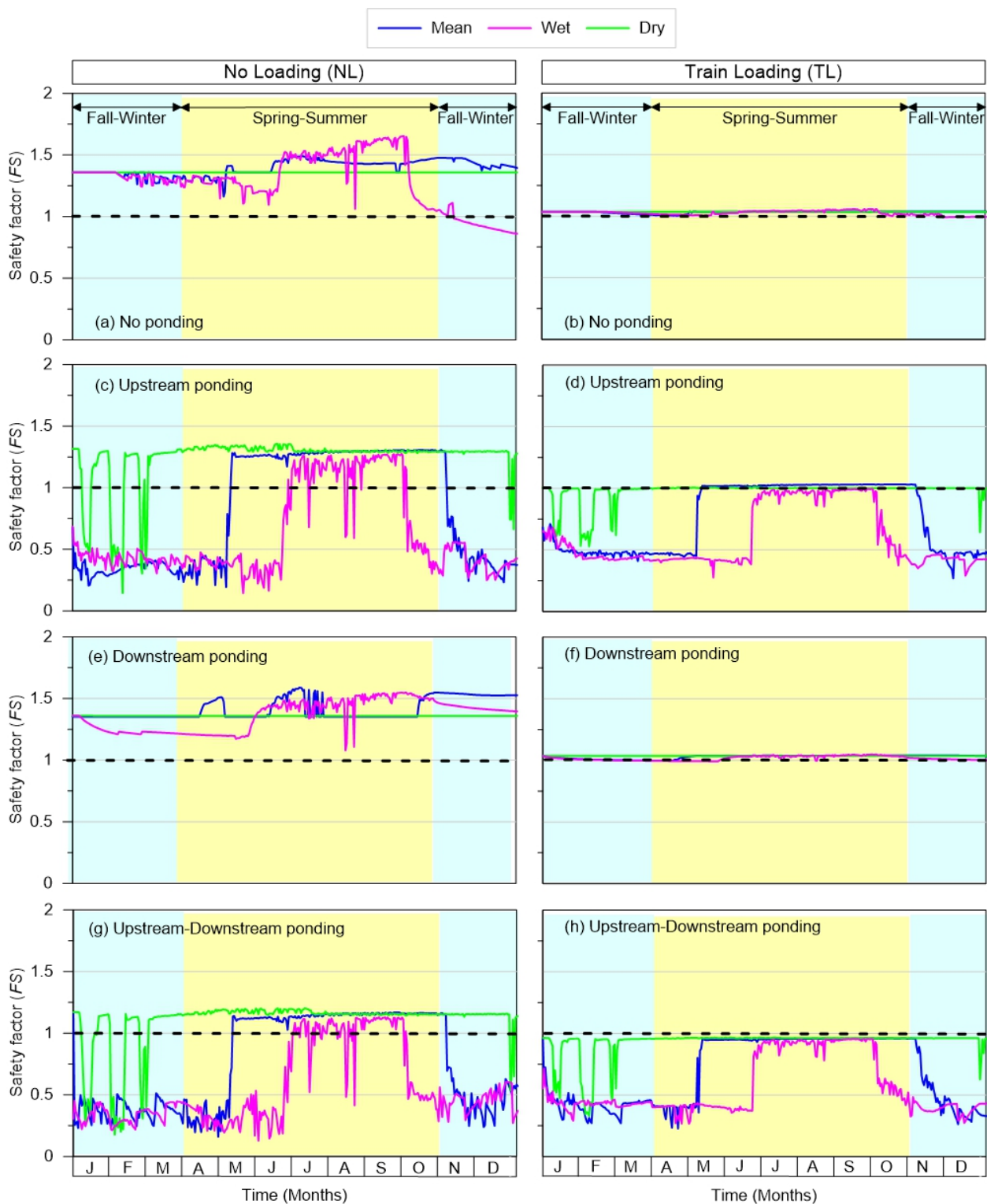
**Figure 8.** Transient *FS* for low embankment at the downstream slope under different climatic, ponding, and loading conditions: (**a**) NP-NL; (**b**) NP-TL; (**c**) US-NL; (**d**) US-TL; (**e**) DS-NL; (**f**) DS-TL; (**g**) US-DS-NL; (**h**) US-DS-TL.

The dry climate consists of minimum precipitation, maximum temperature, maximum wind, minimum humidity, and maximum radiation. The various pairs of scenarios under dry climate conditions showed the following. Under NL, the trends for NP (Figure 8a) and DS (Figure 8e) show *FS* = 1.35 throughout the year because of the prevalent unsaturated

conditions. For US (Figure 8c) and US-DS (Figure 8g), the trends are similar to mean conditions such that the window of increased *FS* extended from mid-March and till the end of December. Furthermore, several dips of *FS* < 1 were observed from January to mid-March and at the end of December because of water-form precipitation owing to the imposed above-zero temperature. Such dips were observed for loess in Air Laya, Indonesia [131], and for clay in Regina, Canada [132]. Under TL, *FS* values were reduced to 1.0 and mostly remained constant throughout the year (Figure 8b,f) similar to mean conditions. Finally, for US (Figure 8d) and US-DS (Figure 8h), *FS* trends were similar to mean conditions such that the slope was always failing. Likewise, the extension in the period of increased *FS* was identical to the NL condition (Figure 8c,g), and the range of dips (*FS* < 1) was reduced due to train loading.

Figure 9 shows the transient *FS* at the downstream slope under different climatic conditions applied to the high embankment (Figure 3a) for various ponding and loading scenarios (Table 1). The various pairs of scenarios under mean climate conditions gave the following results. The trends for NP-NL (Figure 9a) and DS-NL (Figure 9e) show that *FS* varied between 1.35 and 1.45 throughout the year. In comparison with the low embankment, the lower *FS* fluctuations in the larger slope are attributed to the lower ratio of the zone of infiltration to the slope geometry [133]. For US-NL (Figure 9c) and US-DS-NL (Figure 9g), *FS* gradually decreased from 1.35 to 0.75 till the end of April, followed by an abrupt increase to 1.35; it remained constant till November, and gradually reduced back to 0.75. The higher *FS* values in the larger slope, compared to the low embankment, are attributed to the added resistance provided by the increased base length [134]. The *FS* reduced to 1.1 and remained constant for the entire year for NP-TL (Figure 9b) and DS-TL (Figure 9f), similar to the low embankment. Finally, for US-TL (Figure 9d) and US-DS-TL (Figure 9h), *FS* was around 1 ± 0.05 most of the year, with a clear decrease to 0.5 by the end of the year in the latter case. Similar to the low embankment, the trends are subdued and show mostly safe conditions owing to the reduced saturation depth and the high resisting moment in the larger slope.

The various pairs of scenarios under wet climate conditions indicated the following. The trends for NP-NL (Figure 9a) and DS-NL (Figure 9e) show that *FS* variation was similar to mean conditions (1.35 > *FS* > 1.5) for most of the year, albeit with some dips of *FS* ≤ 1 during July and August. The lower fluctuation and higher *FS* is due to the reduced influence of the climate boundary in the high embankment [135]. For US-NL (Figure 9c) and US-DS-NL (Figure 9g), the trends and *FS* values were similar to mean conditions such that the *FS* < 1 period was extended till the end of June and the *FS* > 1 period was reduced to end of September. These trends in the high embankment are similar to the previous case with relatively higher *FS* values. The *FS* was 1.1 for NP-TL (Figure 9b) and DS-TL (Figure 9f), similar to mean conditions and higher than the low embankments. Finally, for US-TL (Figure 9d) and US-DS-TL (Figure 9h), when compared with mean climate conditions, the *FS* ≤ 1 period was extended till the end of June and the *FS* >1 period was reduced till the end of September. Although these trends are similar to the low embankment, the higher slopes are mostly stable over time.

The various pairs of scenarios under dry climate conditions indicated the following. For all ponding scenarios under NL, a constant *FS* value of 1.35 was observed throughout the year owing to dominant unsaturated conditions. The initial fluctuations in US-NL (Figure 9c) and US-DS-NL (Figure 9g), which were previously observed under the low embankment, were not seen because of the reduced ratio of the zone of infiltration to the slope geometry [133]. Likewise, all ponding scenarios under TL showed a constant *FS* of 1.1 for the entire year with no fluctuations.
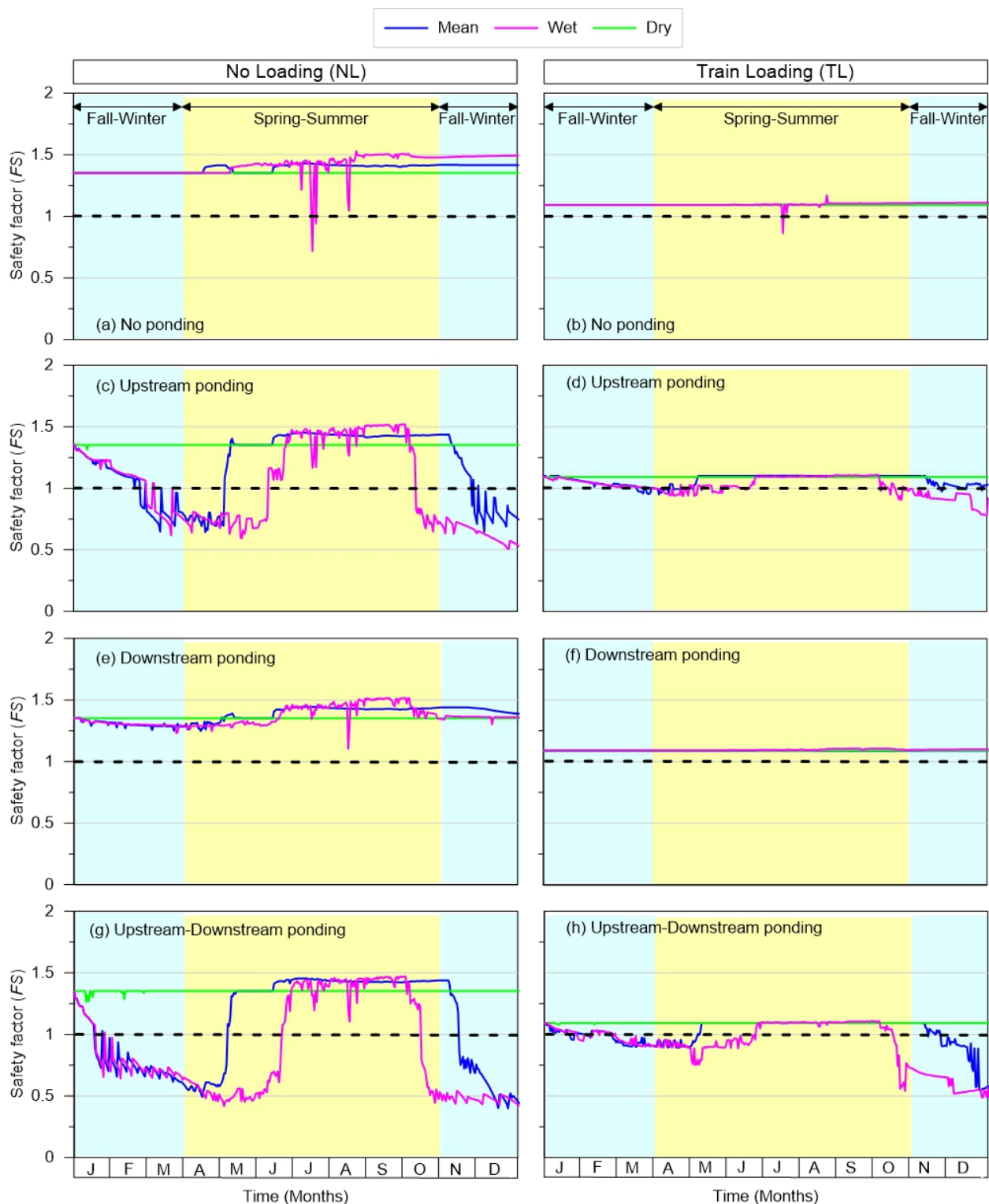
**Figure 9.** Transient *FS* for high embankment at the downstream slope under different climatic, ponding, and loading conditions: (**a**) NP-NL; (**b**) NP-TL; (**c**) US-NL; (**d**) US-TL; (**e**) DS-NL; (**f**) DS-TL; (**g**) US-DS-NL; (**h**) US-DS-TL.

## 5. Summary and Conclusions

Knowledge of weather-induced flow is critical to the integrity of civil infrastructure supported by cohesionless soils. Departing from conventional slope stability analysis, which assumes complete soil saturation as the worst case condition, this research develops

a transient model that coupled two-dimensional flow (hydraulic and thermal) to evaluate slope stability over the various seasons of the year. Using a thoroughly validated model for a semi-arid continental climate, two slope geometries (low with 18 m height and high with 26 m height) were subjected to three weather scenarios (mean, extreme wet, and extreme dry) and four combinations of ponding on the upstream and downstream sides of the slopes under two loads (none and train loading). The main findings of this research are summarized as follows:

- For mean climate conditions, *FS* trends fluctuate till April, followed by an increase that remains constant up to November and decreases thereafter. Generally, the *FS* shows subdued fluctuations and higher values for the high slope when compared with the low slope.
- For wet climate conditions, the *FS* patterns are similar to mean conditions albeit with reduced durations of stability during the summer; for dry climate conditions, *FS* values are higher than mean conditions and nearly constant most of the year.
- For no ponding and downstream ponding, *FS* > 1 throughout the year. In contrast, *FS* > 1 only during the summer (with reduced time in wet climate and extended time in dry climate conditions) for upstream ponding and both upstream–downstream ponding.
- For train loading, *FS* show subdued fluctuations and lower values than the corresponding no-loading scenarios for both slopes. The effect of climatic conditions and ponding scenarios was further reduced for high slopes.

This parametric analysis provides baseline information required for the design and performance of natural slopes and embankments in cohesionless soils based on the atmospheric conditions prevalent in the Canadian Prairies. The results of the study are useful in optimizing the initial design with respect to saturated–unsaturated soil properties, as well as in forecasting the performance of slopes under climatic conditions over the operational life of civil infrastructure. For site-specific applications, the model should be extended to capture the limitations related to the following points: (i) soil heterogeneity and anisotropy—the slope profile may comprise geologically layered soils or different types of borrow materials used for construction such that in both cases, the variable hydraulic and thermal properties of the earthen materials will affect seepage and stability; (ii) surface cover and slope protection—traffic, vegetation, stone pitching, and concrete at the surface and along the slope affect runoff, infiltration, evaporation, and evapotranspiration, thereby influencing stability; (iii) groundwater and perched water—high levels of groundwater due to a nearby lake or river or perched water due to a relatively impermeable zone within the slope will significantly affect flow through and stability; and (iv) seasonal weather and climate scenarios—seasonal weather extremes such as flash floods and heat waves and several other combinations of atmospheric parameters can be considered to predict seepage and stability under critical scenarios.

# References

1. Li, P.; Vanapalli, S.K.; Li, T. Review of Collapse Triggering Mechanism of Collapsible Soils Due to Wetting. *J. Rock Mech. Geotech. Eng.* **2016**, *8*, 256–274. [CrossRef]
2. Wickens, G.E. *Ecophysiology of Economic Plants in Arid and Semi-Arid Land*; Springer: New York, NY, USA, 1998.
3. Houston, S.L. Characterization of Unsaturated Soils: The Importance of Response to Wetting. In Proceedings of the Geo-Congress 2014 Keynote Lectures: Geo-Characterization and Modeling for Sustainability, Atlanta, GA, USA, 23–26 February 2014; pp. 77–96.
4. Jefferson, I.; Rogers, C.D. Collapsible Soils. *ICE Man. Geotech. Eng.* **2012**, *1*, 391–411.
5. Ravindran, S.; Gratchev, I. Effect of Water Content on Apparent Cohesion of Soils from Landslide Sites. *Geotechnics* **2022**, *2*, 385–394. [CrossRef]
6. Areco, P.; Li, Y.; Eguez, C.M.; Fuentes, M.J.R. *Afsluitdijk Upgrading-Non Typical Dutch Solutions*; T U Delft: Delft, The Netherlands, 2013.
7. Wichman, B.; Knoeff, J.G.; de Vries, G. Geotechnical Aspects of Reinforcement Alternatives of the Afsluitdijk. In Proceedings of the 17th International Conference on Soil Mechanics and Geotechnical Engineering (Volumes 1, 2, 3 and 4), Alexandria, Egypt, 5–9 October 2009; IOS Press: Amsterdam, The Netherlands, 2009; pp. 1514–1517.
8. Bush, E.; Lemmen, D.S. *Canada's Changing Climate Report*; Government of Canada: Ottawa, ON, Canada, 2019.
9. Vincent, L.A.; Zhang, X.; Mekis, É.; Wan, H.; Bush, E.J. Changes in Canada's Climate: Trends in Indices Based on Daily Temperature and Precipitation Data. *Atmos. Ocean.* **2018**, *56*, 332–349. [CrossRef]
10. Eekhout, J.P.; de Vente, J. Global Impact of Climate Change on Soil Erosion and Potential for Adaptation through Soil Conservation. *Earth-Sci. Rev.* **2022**, *226*, 103921. [CrossRef]
11. Fan, X.; Dufresne, A.; Subramanian, S.S.; Strom, A.; Hermanns, R.; Stefanelli, C.T.; Hewitt, K.; Yunus, A.P.; Dunning, S.; Capra, L. The Formation and Impact of Landslide Dams–State of the Art. *Earth-Sci. Rev.* **2020**, *203*, 1–28. [CrossRef]
12. Chen, X.; Cui, P.; You, Y.; Cheng, Z.; Khan, A.; Ye, C.; Zhang, S. Dam-Break Risk Analysis of the Attabad Landslide Dam in Pakistan and Emergency Countermeasures. *Landslides* **2017**, *14*, 675–683. [CrossRef]
13. Wartman, J.; Montgomery, D.R.; Anderson, S.A.; Keaton, J.R.; Benoît, J.; dela Chapelle, J.; Gilbert, R. The 22 March 2014 Oso Landslide, Washington, USA. *Geomorphology* **2016**, *253*, 275–288. [CrossRef]
14. Gaur, M.K.; Squires, V.R. Geographic Extent and Characteristics of the World's Arid Zones and Their Peoples. *Clim. Var. Impacts Land Use Livelihoods Drylands* **2018**, *1*, 3–20.
15. Qader, S.H.; Dash, J.; Alegana, V.A.; Khwarahm, N.R.; Tatem, A.J.; Atkinson, P.M. The Role of Earth Observation in Achieving Sustainable Agricultural Production in Arid and Semi-Arid Regions of the World. *Remote Sens.* **2021**, *13*, 3382. [CrossRef]
16. Xie, W.; Li, P.; Zhang, M.; Cheng, T.; Wang, Y. Collapse Behavior and Microstructural Evolution of Loess Soils from the Loess Plateau of China. *J. Mt. Sci.* **2018**, *15*, 1642–1657. [CrossRef]
17. Geertsema, M.; Highland, L.; Vaugeouis, L. Environmental Impact of Landslides. *Landslides–Disaster Risk Reduct.* **2009**, *1*, 589–607.
18. Montgomery, D.R.; Massong, T.M.; Hawley, S.C. Influence of Debris Flows and Log Jams on the Location of Pools and Alluvial Channel Reaches, Oregon Coast Range. *Geol. Soc. Am. Bull.* **2003**, *115*, 78–88. [CrossRef]
19. Sams, C. Impact of Landslides on Environment. *J. Sci. Geosci.* **2022**, *10*, 1–2.
20. Schuster, R.L.; Highland, L.M. Overview of the Effects of Mass Wasting on the Natural Environment. *Environ. Eng. Geosci.* **2007**, *13*, 25–44. [CrossRef]
21. Acton, D.F.; Bedard-Haughn, A. Prairie. The Canadian Encyclopedia. 2015. Available online: https://www.thecanadianencyclopedia.ca/en/article/prairie (accessed on 20 August 2023).
22. City of Calgary. *Flooding in Calgary—Flood of 2013*; Government of Alberta: Edmonton, AB, Canada, 2013.
23. Public Safety Canada. *Floods*; Government of Canada: Ottawa, ON, Canada, 2022.
24. AGR. *Current Drought Conditions-Canadian Drought Monitor*; Government of Canada: Ottawa, ON, Canada, 2023.
25. Canada Dam Association. Inventory of Large Dams in Canada. In Proceedings of the 87th Annual Meeting and Symposium of the International Commission on Large Dams (ICOLD), Ottawa, ON, Canada, 9–14 June 2019.
26. Parizot, M. A counting of tailings in Canada. CIM Magazine. 2020. Available online: https://magazine.cim.org/en/tailings/a-counting-of-tailings-in-canada/ (accessed on 21 August 2023).
27. Suchan, J.; Azam, S. Effect of Salinity on Evaporation from Water Surface in Bench-Scale Testing. *Water* **2021**, *13*, 2067. [CrossRef]
28. Ur Rehman, Z.; Khalid, U.; Ijaz, N.; Mujtaba, H.; Haider, A.; Farooq, K.; Ijaz, Z. Machine Learning-Based Intelligent Modeling of Hydraulic Conductivity of Sandy Soils Considering a Wide Range of Grain Sizes. *Eng. Geol.* **2022**, *311*, 106899. [CrossRef]
29. Porter, M.; Van Hove, J.; Barlow, P.; Froese, C.; Bunce, C. The Estimated Economic Impacts of Prairie Landslides in Western Canada. In Proceedings of the 72nd Canadian Geotechnical Conference, St. John's, NL, Canada, 2 October 2019.
30. Leishman, E.M. Analysis of Canadian Train Derailments from 2001 to 2014. Master's Thesis, University of Alberta, Edmonton, AB, Canada, 2017.
31. Kelly, A.J.; Antunes, P.J.; Vu, H.Q.; Clifton, A.W.; Widger, R.A.; King, G.L. Analysis of Multiple Landslide Blocks on a Highway Crossing of the Frenchman River Valley, Saskatchewan. In Proceedings of the 58th Geotechnical Conference, Saskatoon, SK, Canada, 18–21 September 2005.
32. Transportation Safety Board. *Natural Gas Pipeline Rupture, Manitoba*; Report P14H0011; Transportation Safety Board of Canada: Gatineau, QC, Canada, 2014.
33. Kost, H. Bassano Dam Emergency Spillway Completed. *CBC News*, 25 October 2019.

34. Government of Manitoba Province Recommending Evacuation of People and Livestock from Specific Properties Downstream of Rivers Dam. Available online: https://news.gov.mb.ca/news/index.html?item=48548 (accessed on 31 August 2023).

35. PAS. *Saskatchewan Watershed Authority-Dam Safety Report*; Report submitted to Government of Saskatchewan: Regina, SK, Canada, 2005.

36. Water Security Agency. *Map of Dams*; Government of Saskatchewan: Regina, SK, Canada, 2023.

37. Henschel, M.D.; Deschamps, B.; Robert, G.; Zulkoski, D. Preliminary Monitoring of Ground Slumping Across a Natural Gas Distribution Network with Satellite Radar. In Proceedings of the International Pipeline Conference, American Society of Mechanical Engineers, Calgary, AB, Canada, 26–30 September 2016; Volume 50275, pp. 1–6.

38. Huang, Q.; Akram, I.; Azam, S. *Geohazard Evaluation at South Lake*; SaskEnergy: Swift Current, SK, Canada, 2019.

39. Clifton Associates. *Upper Qu'Appelle Water Supply Project -Economic Impact & Sensitivity Analysis*; Government of Saskatchewan: Regina, SK, Canada, 2012.

40. SNC-Lavalin. *Saskatoon Freeway Functional Planning Study*; Government of Saskatchewan: Regina, SK, Canada, 2019.

41. Greco, R.; Gargano, R. A Novel Equation for Determining the Suction Stress of Unsaturated Soils from the Water Retention Curve Based on Wetted Surface Area in Pores. *Water Resour. Res.* **2015**, *51*, 6143–6155. [CrossRef]

42. Zhu, Y.; Ishikawa, T.; Subramanian, S.S.; Luo, B. Simultaneous Analysis of Slope Instabilities on a Small Catchment-Scale Using Coupled Surface and Subsurface Flows. *Eng. Geol.* **2020**, *275*, 105750. [CrossRef]

43. Lu, N.; Likos, W.J. *Unsaturated Soil Mechanics*; John Wiley and Sons Inc.: New York, NY, USA, 2004.

44. Suchan, J.; Azam, S. Determination of Evaporative Fluxes Using a Bench-Scale Atmosphere Simulator. *Water* **2021**, *13*, 84. [CrossRef]

45. Andersland, O.B.; Ladanyi, B. *Frozen Ground Engineering*; John Wiley and Sons Inc.: New York, NY, USA, 2004.

46. Tissen, C.; Menberg, K.; Bayer, P.; Blum, P. Meeting the Demand: Geothermal Heat Supply Rates for an Urban Quarter in Germany. *Geotherm. Energy* **2019**, *7*, 9. [CrossRef]

47. Uchaipichat, A.; Khalili, N. Experimental Investigation of Thermo-Hydro-Mechanical Behaviour of an Unsaturated Silt. *Géotechnique* **2009**, *59*, 339–353. [CrossRef]

48. Konrad, J.-M. Freezing-Induced Water Migration in Compacted Base-Course Materials. *Can. Geotech. J.* **2008**, *45*, 895–909. [CrossRef]

49. Konrad, J.-M.; Morgenstern, N.R. A Mechanistic Theory of Ice Lens Formation in Fine-Grained Soils. *Can. Geotech. J.* **1980**, *17*, 473–486. [CrossRef]

50. Farouki, O.T. *Thermal Properties of Soils*; Cold Regions Research and Engineering Lab Hanover NH.: Hanover, NH, USA, 1981.

51. Harlan, R.L. Analysis of Coupled Heat-Fluid Transport in Partially Frozen Soil. *Water Resour. Res.* **1973**, *9*, 1314–1323. [CrossRef]

52. Johansen, O. *Thermal Conductivity of Soils*; Cold Regions Research and Engineering Lab Hanover NH.: Hanover, NH, USA, 1977.

53. Nixon, J.F. Discrete Ice Lens Theory for Frost Heave in Soils. *Can. Geotech. J.* **1991**, *29*, 843–859. [CrossRef]

54. Tsegaye, A.B. *Simple Models for Frozen Soil. Modeling the Strength of Saturated Frozen Soil*; Norwegian University of Science and Technology: Trondheim, Norway, 2014.

55. Gasmo, J.M.; Rahardjo, H.; Leong, E.C. Infiltration Effects on Stability of a Residual Soil Slope. *Comput. Geotech.* **2000**, *26*, 145–165. [CrossRef]

56. Oswaldo, A.F.; Fernandes, M.A. Landslide Analysis of Unsaturated Soil Slopes Based on Rainfall and Matric Suction Data. *Bull. Eng. Geol. Environ.* **2019**, *78*, 4167–4185.

57. Zhang, L.L.; Zhang, L.M.; Tang, W.H. Rainfall-Induced Slope Failure Considering Variability of Soil Properties. *Geotechnique* **2005**, *55*, 183–188. [CrossRef]

58. Qin, Z.; Lai, Y.; Tian, Y.; Zhang, M. Stability Behavior of a Reservoir Soil Bank Slope under Freeze-Thaw Cycles in Cold Regions. *Cold Reg. Sci. Technol.* **2021**, *181*, 103181. [CrossRef]

59. Shin, Y.; Choi, J.C.; Quinteros, S.; Svendsen, I.; L'Heureux, J.S.; Seong, J. Evaluation and Monitoring of Slope Stability in Cold Region: Case Study of Man-Made Slope at Øysand, Norway. *Appl. Sci.* **2020**, *10*, 4136. [CrossRef]

60. Batenipour, H.; Alfaro, M.; Kurz, D.; Graham, J. Deformations and Ground Temperatures at a Road Embankment in Northern Canada. *Can. Geotech. J.* **2014**, *51*, 260–271. [CrossRef]

61. Zhu, Y.; Ishikawa, T.; Yamada, T.J.; Subramanian, S.S. Probability Assessment of Slope Instability in Seasonally Cold Regions under Climate Change. *J. Infrastruct. Preserv. Resil.* **2021**, *2*, 1–15. [CrossRef]

62. Rodríguez, S.; Puig i Polo, C.; Lloret Morancho, A.; Vaunat, J.; Hurlimann Ziegler, M. Effect of Climate Change on Slope Stability: A Numerical Analysis Using Predictions of the Catalan Pyrenees. In Proceedings of the 13th International Symposium on Landslides, Cartagena, Colombia, 22–26 February 2021; ISSMGE: London, UK, 2021; pp. 1–8.

63. Subramanian, S.S.; Ishikawa, T.; Tokoro, T. Stability Assessment Approach for Soil Slopes in Seasonal Cold Regions. *Eng. Geol.* **2017**, *221*, 154–169. [CrossRef]

64. Korshunov, A.A.; Doroshenko, S.P.; Nevzorov, A.L. The Impact of Freezing-Thawing Process on Slope Stability of Earth Structure in Cold Climate. *Procedia Eng.* **2016**, *143*, 682–688. [CrossRef]

65. Gariano, S.L.; Rianna, G.; Petrucci, O.; Guzzetti, F. Assessing Future Changes in the Occurrence of Rainfall-Induced Landslides at a Regional Scale. *Sci. Total Environ.* **2017**, *596*, 417–426. [CrossRef]

66. Alvioli, M.; Melillo, M.; Guzzetti, F.; Rossi, M.; Palazzi, E.; von Hardenberg, J.; Brunetti, M.T.; Peruccacci, S. Implications of Climate Change on Landslide Hazard in Central Italy. *Sci. Total Environ.* **2018**, *630*, 1528–1543. [CrossRef]

67.  Subramanian, S.S.; Ishikawa, T.; Tokoro, T. An Early Warning Criterion for the Prediction of Snowmelt-Induced Soil Slope Failures in Seasonally Cold Regions. *Soils Found.* **2018**, *58*, 582–601. [CrossRef]
68.  Tang, Y.; Wu, W.; Yin, K.; Wang, S.; Lei, G. A Hydro-Mechanical Coupled Analysis of Rainfall Induced Landslide Using a Hypoplastic Constitutive Model. *Comput. Geotech.* **2019**, *112*, 284–292. [CrossRef]
69.  Mateos, R.M.; García-Moreno, I.; Azañón, J.M. Freeze–Thaw Cycles and Rainfall as Triggering Factors of Mass Movements in a Warm Mediterranean Region: The Case of the Tramuntana Range (Majorca, Spain). *Landslides* **2012**, *9*, 417–432. [CrossRef]
70.  Zhou, J.; Cui, P.; Hao, M. Comprehensive Analyses of the Initiation and Entrainment Processes of the 2000 Yigong Catastrophic Landslide in Tibet, China. *Landslides* **2016**, *13*, 39–54. [CrossRef]
71.  Bahrami, S.; Ardejani, F.D.; Baafi, E. Application of Artificial Neural Network Coupled with Genetic Algorithm and Simulated Annealing to Solve Groundwater Inflow Problem to an Advancing Open Pit Mine. *J. Hydrol.* **2016**, *536*, 471–484. [CrossRef]
72.  Ijaz, N.; Ye, W.; ur Rehman, Z.; Dai, F.; Ijaz, Z. Numerical Study on Stability of Lignosulphonate-Based Stabilized Surficial Layer of Unsaturated Expansive Soil Slope Considering Hydro-Mechanical Effect. *Transp. Geotech.* **2022**, *32*, 100697. [CrossRef]
73.  Geo-Slope. *Thermal Modeling with TEMP/W: An Engineering Methodology*; GEO-SLOPE International Ltd.: Calgary, AB, Canada, 2020.
74.  Alsherif, N.; Wayllace, A.; Lu, N. Measuring the Soil Water Retention Curve under Positive and Negative Matric Suction Regimes. *Geotech. Test. J.* **2015**, *38*, 442–451. [CrossRef]
75.  Wayllace, A.; Lu, N. A Transient Water Release and Imbibitions Method for Rapidly Measuring Wetting and Drying Soil Water Retention and Hydraulic Conductivity Functions. *Geotech. Test. J.* **2012**, *35*, 1–15.
76.  Vanapalli, S.K.; Lane, J.J. A Simple Technique for Determining the Shear Strength of Finegrained Unsaturated Soils Using the Conventional Direct Shear Apparatus. In Proceedings of the Second Canadian Specialty Conference on Computer Applications in Geotechnique, Winnipeg, MB, Canada, 28–30 April 2002; pp. 245–253.
77.  Mahmood, K.; Kim, J.M.; Ashraf, M. Ziaurrehman The Effect of Soil Type on Matric Suction and Stability of Unsaturated Slope under Uniform Rainfall. *KSCE J. Civ. Eng.* **2016**, *20*, 1294–1299. [CrossRef]
78.  GeoSlope. *Stability Modeling with GeoStudio*; GEO-SLOPE International Ltd.: Calgary, AB, Canada, 2020.
79.  Azmatch, T.F.; Sego, D.C.; Arenson, L.U.; Biggar, K.W. Soil Freezing Characteristic Curve of Devon Silt. In Proceedings of the David C. Sego Symposium, University of Alberta, Edmonton, AB, Canada, 26–27 April 2012; pp. 26–27.
80.  Unold, F.; Derk, L. Cryosuction–a Model to Describe the Mechanism during Ground Freezing. In *PanAm Unsaturated Soils 2017*; American Society of Civil Engineers: Reston, VA, USA, 2017; pp. 290–299.
81.  Stuurop, J.C.; van der Zee, S.E.M.; Voss, C.I.; French, H.K. Simulating Water and Heat Transport with Freezing and Cryosuction in Unsaturated Soil: Comparing an Empirical, Semi-Empirical and Physically-Based Approach. *Adv. Water Resour.* **2021**, *149*, 103846. [CrossRef]
82.  Flerchinger, G.N.; Seyfried, M.S.; Hardegree, S.P. Using Soil Freezing Characteristics to Model Multi-Season Soil Water Dynamics. *Vadose Zone J.* **2006**, *5*, 1143–1153. [CrossRef]
83.  Morgenstern, N.R.U.; Price, V.E. The Analysis of the Stability of General Slip Surfaces. *Geotechnique* **1965**, *15*, 79–93. [CrossRef]
84.  Ward, N. Geography of Saskatchewan. The Canadian Encyclopedia. 2023. Available online: https://www.thecanadianencyclopedia.ca/en/article/geography-of-saskatchewan (accessed on 20 August 2023).
85.  StatCan. *Focus on Geography-Population Change in Province and Terri Tories*; Government of Canada: Ottawa, ON, Canada, 2016.
86.  Azam, S.; Khan, F. Geohydrological Properties of Selected Badland Sediments in Saskatchewan, Canada. *Bull. Eng. Geol. Environ.* **2014**, *73*, 389–399. [CrossRef]
87.  Wittrock, V. *Cliamte Reference Station-Conservation Learning Center*; Saskatchewan Research Council: Saskatoon, SK, Canada, 2023.
88.  Aguiar, M. Vegetation and Soil Biodiversity Across Perennial Grassland-Annual Cropland Edges. Ph.D. Thesis, University of Saskatchewan, Saskatoon, SK, Canada, 2019.
89.  Infoplease Saskatchewan Map | Infoplease. Available online: https://www.infoplease.com/atlas/north-america/canada/saskatchewan-map (accessed on 1 September 2023).
90.  Map Trove Where Is Saskatchewan? Available online: https://www.maptrove.ca/info/where/canada/saskatchewan (accessed on 1 September 2023).
91.  Darve, F.; Laouafa, F. Plane Strain Instabilities in Soil: Application to Slopes Stability. In *Numerical Models in Geomechanics*; CRC Press: Boca Raton FL, USA, 2020; pp. 85–90.
92.  Gitirana, J.G. Weather-Related Geo-Hazard Assessment Model for Railway Embankment Stability. PhD Thesis, University of Saskatchewan, Saskatoon, SK, Canada, 2005.
93.  de Gitirana, G.F.; Fredlund, D.G. The Application of Unsaturated Soil Mechanics to the Assessment of Weather-Related Geo-Hazards. In Proceedings of the 16th International Conference on Soil Mechanics and Geotechnical Engineering, Osaka, Japan, 12–16 September 2005; IOS Press: Amsterdam, The Netherlands, 2005; pp. 2515–2520.
94.  Akram, I.; Azam, S. Determination of Saturated-Unsaturated Flow through Silty Sand. *Geotech. Geol. Eng.* **2022**, *40*, 469–481. [CrossRef]
95.  Mitchell, J.K.; Soga, K. *Fundamentals of Soil Behavior*; John Wiley and Sons Inc.: New York, NY, USA, 2005.
96.  *ASTM-D2487*; Standard Practice for Classification of Soils for Engineering Purposes (Unified Soil Classification System). West Conshohocken: Montgomery, PA, USA, 2017.

97. Newman, G.P. Heat and Mass Transfer in Unsaturated Soils during Freezing. Master's Thesis, University of Saskatchewan, Saskatoon, SK, Canada, 1995.

98. De Vries, D.A. Heat Transfer in Soils, Heat and Mass Transfer in the Bioaphere. *Adv. Therm. Exgineerings* **1975**, *1*, 5–28.

99. Akram, I.; Azam, S. Effect of Sample Preparation on Saturated and Unsaturated Shear Strength of Cohesionless Soils. *Geotechnics* **2023**, *3*, 212–223. [CrossRef]

100. Li, Z.; Wang, S.; Li, J. Spatial Variations and Long-Term Trends of Potential Evaporation in Canada. *Sci. Rep.* **2020**, *10*, 22089. [CrossRef] [PubMed]

101. Sauchyn, D.; Kulshreshtha, S. Prairies. In *From Impacts to Adaptation: Canada in a Changing Climate*; Natural Resources Canada: Ottawa, ON, Canada, 2008.

102. Sauchyn, D.; Barrow, E.; Fang, X.; Henderson, N.; Johnston, M.; Pomeroy, J. *Saskatchewan's Natural Capital in a Changing Climate: An Assessment of Impacts and Adaptation*; Saskatchewan Ministry of Environment: Regina, SK, Canada, 2009.

103. Saskatchewan Research Council. *Monthly Climate Data Report*; Saskatchewan Research Council Climate: Saskatoon, SK, Canada, 2021.

104. Environment Canada. *Environment Canada Climate Normals (1981–2008)*; Government of Canada: Ottawa, ON, Canada, 2014.

105. Tang, R.; Zhou, G.; Jiao, W.; Ji, Y. Theoretical Model of Hydraulic Conductivity for Frozen Saline/Non-Saline Soil Based on Freezing Characteristic Curve. *Cold Reg. Sci. Technol.* **2019**, *165*, 102794. [CrossRef]

106. Fang, X.; Pomeroy, J.W. Snowmelt Runoff Sensitivity Analysis to Drought on the Canadian Prairies. *Hydrol. Process.* **2007**, *21*, 2594–2609. [CrossRef]

107. McGinn, S.M. Weather and Climate Patterns in Canada's Prairie Grasslands. *Arthropods Can. Grassl.* **2010**, *1*, 105–119.

108. Vickers, G.; Buzza, S.; Schmidt, D.; Mullock, J. *The Weather of the Canadian Prairies*; NAV: Ottawa, ON, Canada, 2002.

109. Basu, S.; Sauchyn, D.J. Future Changes in the Surface Water Balance over Western Canada Using the CanESM5 (CMIP6) Ensemble for the Shared Socioeconomic Pathways 5 Scenario. *Water* **2022**, *14*, 691. [CrossRef]

110. Pomeroy, J.W.; Fang, X.; Williams, B. *Impacts of Climate Change on Saskatchewan's Water Resources*; Centre of Hydrology, University of Saskatchewan: Saskatoon, SK, Canada, 2009.

111. Barrow, E. *Climate Scenarios for Saskatchewan*; Prairie Adaptation Research Collaborative Report; University of Regina: Regina, SK, Canada, 2009.

112. Akhter, A.; Azam, S. Flood-Drought Hazard Assessment for a Flat Clayey Deposit in the Canadian Prairies. *J. Environ. Inform. Lett.* **2019**, *1*, 8–19. [CrossRef]

113. Bonsal, B.R.; Cuell, C.; Wheaton, E.; Sauchyn, D.J.; Barrow, E. An Assessment of Historical and Projected Future Hydro-Climatic Variability and Extremes over Southern Watersheds in the Canadian Prairies. *Int. J. Climatol.* **2017**, *37*, 3934–3948. [CrossRef]

114. Paranthaman, R.; Azam, S. Coupled Hydraulic-Thermal Model for Soils under Extreme Weather in Cold Regions. *J. Environ. Inform. Lett.* **2022**, *7*, 90–102. [CrossRef]

115. Pei, Z.; Fang, S.; Wang, L.; Yang, W. Comparative Analysis of Drought Indicated by the SPI and SPEI at Various Timescales in Inner Mongolia, China. *Water* **2020**, *12*, 1925. [CrossRef]

116. Nam, W.-H.; Hayes, M.J.; Svoboda, M.D.; Tadesse, T.; Wilhite, D.A. Drought Hazard Assessment in the Context of Climate Change for South Korea. *Agric. Water Manag.* **2015**, *160*, 106–117. [CrossRef]

117. Kottek, M.; Grieser, J.; Beck, C.; Rudolf, B.; Rubel, F. World Map of the Köppen-Geiger Climate Classification Updated. *Meteorol. Zeitschrif* **2006**, *15*, 259–263. [CrossRef] [PubMed]

118. Mujtaba, H.; Shimobe, S.; Farooq, K.; ur Rehman, Z.; Khalid, U. Relating Gradational Parameters with Hydraulic Conductivity of Sandy Soils: A Renewed Attempt. *Arab. J. Geosci.* **2021**, *14*, 1–17. [CrossRef]

119. Puri, N.; Prasad, H.D.; Jain, A. Prediction of Geotechnical Parameters Using Machine Learning Techniques. *Procedia Comput. Sci.* **2018**, *125*, 509–517. [CrossRef]

120. Smith, G.N. *Probability and Statistics in Civil Engineering-An Introduction*; Collins: London, UK, 1986.

121. Pavon, G. Evaluating the Thermal Properties of Soils Based on Measured Ground Temperatures. Master's Thesis, University of Manitoba, Winnipeg, MB, Canada, 2018.

122. Roshankhah, S.; Garcia, A.V.; Carlos Santamarina, J. Thermal Conductivity of Sand–Silt Mixtures. *J. Geotech. Geoenviron. Eng.* **2021**, *147*, 1–9. [CrossRef]

123. Al-Kaisi, M.M.; Lal, R.; Olson, K.R.; Lowery, B. Fundamentals and Functions of Soil Environment. In *Soil Health and Intensification of Agroecosytems*; Al-Kaisi, M.M., Lowery, B., Eds.; Academic Press: Cambridge, MA, USA, 2017; pp. 1–23.

124. Le, A.T.; Wang, L.; Wang, Y.; Li, D. Measurement Investigation on the Feasibility of Shallow Geothermal Energy for Heating and Cooling Applied in Agricultural Greenhouses of Shouguang City: Ground Temperature Profiles and Geothermal Potential. *Inf. Process. Agric.* **2021**, *8*, 251–269. [CrossRef]

125. Singh, R.K.; Sharma, R.V. Numerical Analysis for Ground Temperature Variation. *Geotherm. Energy* **2017**, *5*, 22. [CrossRef]

126. Qiu, H.; Cui, P.; Regmi, A.D.; Hu, S.; Wang, X.; Zhang, Y. The Effects of Slope Length and Slope Gradient on the Size Distributions of Loess Slides: Field Observations and Simulations. *Geomorphology* **2018**, *300*, 69–76. [CrossRef]

127. Miller, G.A.; Teh, S.Y.; Li, D.; Zaman, M.M. Cyclic Shear Strength of Soft Railroad Subgrade. *J. Geotech. Geoenviron. Eng.* **2000**, *126*, 139–147. [CrossRef]

128. Li, D.; Li, L.; Xu, L.; Li, C.; Meng, K.; Gao, Y.; Yang, Z. Stability Analysis of Upstream and Downstream Dam Slopes with Water Level Drawdown Using Response Surface Function. *Geotech. Geol. Eng.* **2022**, *40*, 3107–3123. [CrossRef]

129. Lyu, Z.; Chai, J.; Xu, Z.; Qin, Y.; Cao, J. A Comprehensive Review on Reasons for Tailings Dam Failures Based on Case History. *Adv. Civ. Eng.* **2019**, *2019*, 4159306. [CrossRef]

130. Transportation Safety Board. *Main Track Train Derailment*; Report R18W0237; Transportation Safety Board of Canada: Gatineau, QC, Canada, 2018.

131. Gofar, N.; Lee, M.L.; Asof, M. Transient Seepage and Slope Stability Analysis for Rainfall-Induced Landslide: A Case Study. *Malays. J. Civ. Eng.* **2006**, *18*, 1–13.

132. Huang, Q.; Azam, S. Modeling of Weather-Induced Volumetric Changes in Cracked Expansive Clays. *Geotech. Geol. Eng.* **2023**, *41*, 861–879. [CrossRef]

133. Gallage, C.; Abeykoon, T.; Uchimura, T. Instrumented Model Slopes to Investigate the Effects of Slope Inclination on Rainfall-Induced Landslides. *Soils Found.* **2021**, *61*, 160–174. [CrossRef]

134. Shiferaw, H.M. Study on the Influence of Slope Height and Angle on the Factor of Safety and Shape of Failure of Slopes Based on Strength Reduction Method of Analysis. *Beni-Suef Univ. J. Basic Appl. Sci.* **2021**, *10*, 31. [CrossRef]

135. Zhang, Q.; Wang, L.; Zhang, H. Rainfall Infiltration Process of a Rock Slope with Considering the Heterogeneity of Saturated Hydraulic Conductivity. *Front. Earth Sci.* **2022**, *9*, 804005. [CrossRef]